Supporting information for:

Indoor Air Quality Implications of Germicidal 222 nm Light

Victoria Barber[1,2$*], Matthew B. Goss[1$], Lesly J. Franco Deloya[4], Lexy N. LeMar[5], Yaowei Li[6], Erik Helstrom[1], Manjula Canagaratna[7], Frank N. Keutsch[6,8,9], Jesse H. Kroll[1,5*]

[1]Department of Civil and Environmental Engineering, Massachusetts Institute of Technology, Cambridge, Massachusetts 02139, United States
[2]now at Department of Chemistry and Biochemistry, University of California Los Angeles, Los Angeles, California, 90095
[4]Department of Earth, Atmospheric, and Planetary Sciences, Massachusetts Institute of Technology, Cambridge, Massachusetts 02139, United States
[5]Department of Chemical Engineering, Massachusetts Institute of Technology, Cambridge, Massachusetts 02139, United States
[6]John A. Paulson School of Engineering and Applied Sciences, Harvard University, Cambridge, Massachusetts 02138, United States
[7]Center for Aerosol and Cloud Chemistry, Aerodyne Research Incorporated, Billerica, Massachusetts 01821, United States
[8]Department of Chemistry and Chemical Biology, Harvard University, Cambridge, Massachusetts 02138, United States
[9]Department of Earth and Planetary Sciences, Harvard University, Cambridge, Massachusetts 02138, United States
[$]V.P.B. and M.B.G. contributed equally to this work [*]Corresponding Authors

vbarber@chem.ucla.edu
University of California, Los Angeles
Department of Chemistry and Biochemistry
607 Charles E. Young Drive, East, YH3077B
Los Angeles, CA 90095

jhkroll@mit.edu
Massachusetts Institute of Technology
Department of Civil and Environmental Engineering
77 Massachusetts Avenue, 48-331
Cambridge, MA 02139
617-253-2409

Number of pages: 25

Number of figures: 12

Number of tables: 5

Contents

S1. Experimental Conditions and Methods

S1.1. Calculation of average fluence rate in the chamber

Average fluence rate is estimated numerically using data from the lamp manufacturer[1] and a simple model. A simple model of the chamber is built using 60 unit-boxes per meter to represent the ~0.37 m x ~0.37 m x ~1.14 m chamber. Using fluence rate vs distance and beam angle data provided by the lamp manufacturer, the fluence rate in each unit box is calculated. This relies on fluence rate as a function of distance (inverse-square law), fluence rate as a function of beam angle (data from the manufacturer was fit to a lemniscate of Bernoulli curve), and a hard cutoff beyond the reported maximum beam angle (64˚). The average fluence rate is taken as the average across all boxes. A visual representation of this is included as Figure S1. Based on measurements taken with an Ocean Optics USB4000 Spectrometer, the light was not measurably attenuated by passing through the chamber walls so light transmission into the chamber is assumed to be 100%.

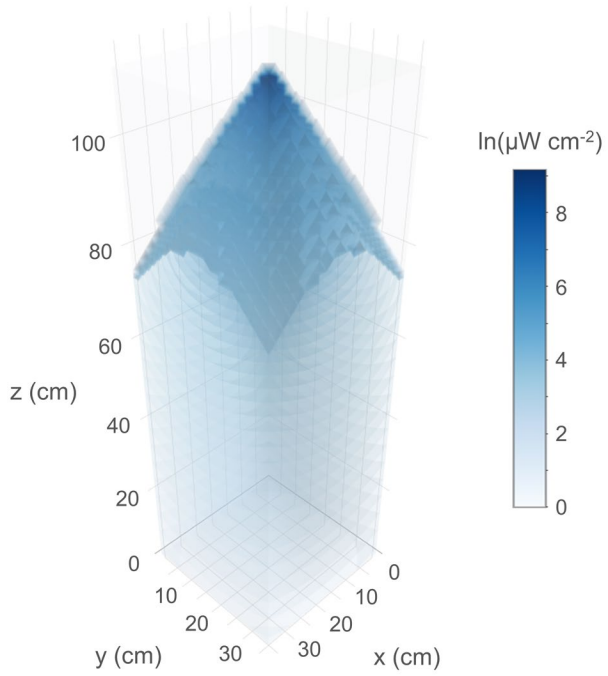

Figure S1: Model output for calculating average chamber fluence rate. The natural logarithm is plotted to allow visualization of lower intensity regions of the chamber.

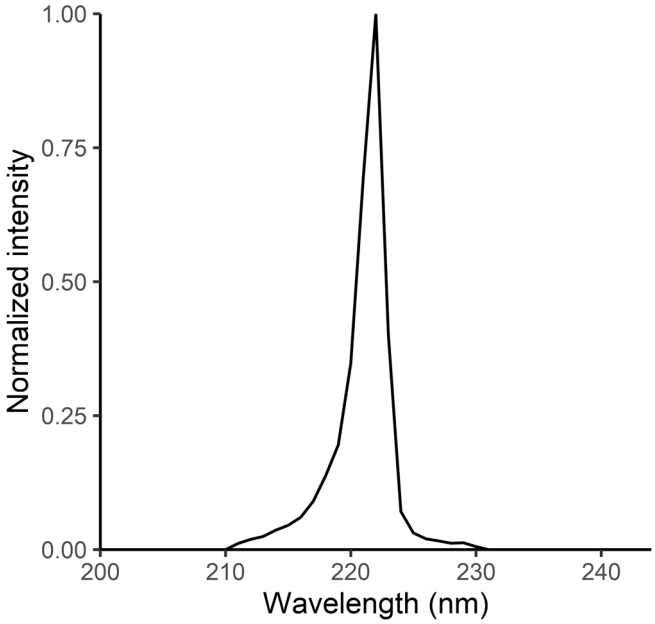

Figure S2: Normalized 222 nm lamp emission spectrum.[2]

Table S1: Summary of experimental conditions, aerosol measurements, and inferred OH. O_3 is measured directly, and is observed to be approximately constant throughout the experiments. Organic aerosol measurements are reported as dilution- and wall-loss-corrected concentrations 30 minutes after the addition of the VOC. Error is reported as the greater of 20% of the concentration or the standard deviation of the concentration from 27 to 33 minutes. OH is inferred from the fits displayed in Figure 2 and S2, the known rate constant for the reaction with OH and hexanal, and the known rate constants for the reactions of OH and cyclohexene and O_3 and cyclohexene.

Precursor VOC	Conditions	Starting Precursor Concentration (ppb)	Fluence rate ($\mu W\ cm^{-2}$)	Ozone* (ppb)	% Relative Humidity*	Organic aerosol ($\mu g\ m^{-3}$)	$[OH]_{avg}$‖, $\times 10^{-6}$ molecules cm^{-3}
Hexanal	Base	10	45	96 ± 2	23.1 ± 0.2	N/A¶	5.0 [4.4, 5.1]
	Elevated VOC	100	45	97 ± 2	22.9 ± 0.2	12 ± 5.2	1.0 [0.4, 1.0]
	O_3 Only	10	0	109 ± 2	27 ± 0.1	1.2 ± 2.4	0.3 [-0.2, 0.3]**
	Higher RH	10	45	105 ± 2	(45)§	6.3 ± 5.1	12.0 [9.7, 12.8]
	Low Light	10	9	24 ± 1	23.6 ± 0.2	1.2 ± 2.1	0.5 [0.4, 0.6]
Cyclohexene	Base	10	45	101 ± 2	(25) §	N/A¶	6.3 [4.9, 7.1]
	Elevated VOC	100	45	92 ± 2	22.6 ± 0.2	37.2 ± 7.4	2.0 [1.9, 2.0]
	O_3 Only	10	0	105 ± 4	25.6 ± 0.1	N/A¶	1.5 [1.4, 2.0]
	Higher RH	10	45	103 ± 2	(45)§	4.5 ± 3	7.3 [5.9, 8.1]
	Low Light	10	9	21 ± 2	20.8 ± 0.1	1.5 ± 4.1	0.6 [0.2, 0.7]
Limonene	Base	10	45	107 ± 2	22.7 ± 0.2	12.4 ± 2.9	N/A††
	Elevated VOC	100	45	91 ± 3†	23.9 ± 0.2	399 ± 79.8#	N/A††
	O_3 Only	10	0	103 ± 2	24 ± 0.2	5.8 ± 4.2	N/A††
	Higher RH	10	45	104 ± 2	(45)§	18.7 ± 3.7	N/A††
	Low Light	10	9	24 ± 1	23.3 ± 0.2	4.3 ± 2.8	N/A††
Blank	Base	-	45	100 ± 2‡	25.5 ± 0.4	0.2 ± 1.7	N/A‡‡
	O_3 only	-	0	103 ± 2‡	24.8 ± 0.2	-1.6 ± 1.4	N/A‡‡
	Low Light	-	9	23 ± 3‡	21.1 ± 0.2	-0.3 ± 0.9	N/A‡‡

*Error is reported as one standard deviation.

†Elevated limonene concentration was sufficient to slightly suppress the steady-state O_3 concentration.

‡These measurements were taken only at the end of the experiment since the experiment started with an ozone-free chamber.

§Data lost due to corrupted file. Reported RH is approximate, based on contemporaneous notes of RH sensor output.

¶No measurement due to instrumental or contamination issues.

#Nucleation that occurred during this experiment increases the error in this measurement and is not reflected in the calculated error.

[||]Values are reported as "mean [minimum, maximum]" where the minimum and maximum values are calculated as described in Section S1.4.
[**]Nonzero derived [OH] for this experiment is likely due to hexanal losses which are not accounted for. See Section S1.2.
[††]Uncertainty in the limonene timeseries prevents determination of [OH] for these experiments.
[‡‡]No precursor was present from which to calculate [OH].

S1.2. Reactant addition

Acetonitrile (5.3 ppb) and 1-butan-d9-ol (1.2 ppb) are introduced via a 6.8 µL addition of aqueous solution containing 2.5 µL and 1 µL respectively in 10 mL water. With literature $k_{OH,\ 298\ K} = 2.3 \times 10^{-14}$, [3] acetonitrile is effectively unreactive under these conditions, and no evidence of photolytic loss is observed. The 1-butan-d9-ol was intended is an OH tracer but OH levels are too low to reliably use it to estimate [OH]. 1-2 minutes later, 120 ± 11 µg m^{-3} of dry ammonium sulfate seed particles are introduced to the chamber using a TSI atomizer (Model 3076), a solution of ammonium sulfate in HPLC water (2 g/L), and a particle dryer (Brechtel 9200). 1-2 minutes later, the reactive VOC is introduced to the chamber via headspace injection. Here, a small amount of the VOC is introduced in liquid form into a closed flask equipped with a rubber septum, and allowed to equilibrate for several minutes. A gas-tight syringe is then use to draw up a volume of the headspace within the flask that, based on the vapor pressure of the VOC, corresponds to the desired concentration within the chamber. Three different VOCs are used, including hexanal ($C_6H_{12}O$, 98%, Sigma Aldrich), cyclohexene (C_6H_{10}, 99%, Sigma Aldrich), and (*R*)-(+)-limonene ($C_{10}H_{16}$, 97%, Sigma Aldrich). For most experiments, 10 ppb of the reactant VOC is targeted as the starting concentration. For three experiments, 100 ppb is used instead to explore the effects of reactant concentration on oxidant concentrations. Because the chamber is at steady-state O_3 and the light is on, chemistry begins immediately upon VOC injection. In all figures, the VOC injection is taken as time = 0. For a full summary of experimental conditions, see Table S1.

Table S2: Summary of analytical instruments used.

Instrument	Manufacturer	Abbreviation	Chemical species measured	Sampling frequency
Vocus proton-transfer reaction mass spectrometer [4]	Aerodyne Research Inc.	Vocus	A range of VOCs, including alkenes and some oxygenated VOCs	1 s^{-1}
Ammonium chemical ionization mass spectrometer [5]	Ionicon Analytik	NH_4^+-CIMS	A broad range of oxygenated VOCs	1 s^{-1}
Aerosol mass spectrometer [6]	Aerodyne Research Inc.	AMS	Particle composition	3 min^{-1}
Scanning mobility particle sizer	TSI	SMPS	Particle size distribution	0.4 min^{-1}
Ozone monitor	2B Technologies	N/A	O_3	6 min^{-1}
NO_X monitor	Thermo Fisher Scientific	N/A	NO, NO_2, NO_X	6 min^{-1}

S1.3. Data analysis

For gas-phase mass spectrometric data, raw Vocus data is processed in Tofware, while raw NH_4^+-CIMS data is processed in PTRwid.[7] Observed ion signals are duty-cycle corrected, background corrected, and then corrected for dilution using the measured decay of the acetonitrile dilution tracer in each experiment. Product ion signals from CIMS instruments are identified using hierarchical clustering[8] to separate signals that increase after the addition of a VOC from signals due to background noise. Results are reported as relative signal, not absolute concentration.

Secondary organic aerosol is quantified by normalizing the AMS Org signal by the ammonium sulfate concentration (see Equation 4 from Wang et al.[9]), and scaled to the initial seed particle mass concentration, as measured by the SMPS. Organic aerosol concentrations are reported in Table S1 as the mean aerosol concentration between 27 and 33 minutes after the injection of the reactive VOC. Error is reported as the greater of either the standard deviation in the signal over this same time period, or 20% of the mean. Nucleation, which may affect the wall-loss corrected concentration, only occurred during the first 30 minutes of the experiment that uses 100 ppb limonene and 222 lights.

S2. Additional Modeling Methods

Table S3: List of reactions used in the 0-D box model. Reactions under "General Reactions" are used in all model configurations. Reactions in the subsequent three sections are only used for modeling cyclohexene experiments, hexanal experiments, and the indoor air scenario respectively. Species contributing to the lumped "VOC1" species for the indoor air scenario are described in Table S4. "VOC2" has the same reactivities as limonene. Note that oxidation products (X_1 and X_2) are considered to have the same OH reactivity as their precursor.

Reaction number	Reaction	Rate ID	Rate	Unit	Citation
	General reactions				
1	$O_2 + hv \rightarrow 2O$	J_1	$4.78 \times 10^{-12} \times I^*$	s^{-1}	[3]
2	$O + O_2 + M \rightarrow O_3 + M$	k_2	1.5×10^{-14}	$cm^3\ molec^{-1}\ s^{-1}$	[10]
3	$H_2O + O(^1D) \rightarrow 2OH$	k_3	2×10^{-10}	$cm^3\ molec^{-1}\ s^{-1}$	[10]
4	$O + O_3 \rightarrow 2O_2$	k_4	8×10^{-15}	$cm^3\ molec^{-1}\ s^{-1}$	[10]
5a	$O_3 + hv \rightarrow (O^1D) + O_2$	J_{5a}	$1.48 \times 10^{-11} \times I^*$	s^{-1}	[3]
5b	$O_3 + hv \rightarrow O + O_2$	J_{5b}	$5.07 \times 10^{-12} \times I^*$	s^{-1}	[3]
6	$OH + O_3 \rightarrow HO_2 + O_2$	k_6	7.25×10^{-14}	$cm^3\ molec^{-1}\ s^{-1}$	[10]
7	$OH + HO_2 \rightarrow H_2O + O_2$	k_7	1.11×10^{-10}	$cm^3\ molec^{-1}\ s^{-1}$	[10]
8	$HO_2 + O_3 \rightarrow OH + 2O_2$	k_8	2.01×10^{-15}	$cm^3\ molec^{-1}\ s^{-1}$	[10]
9	$O(^1D) \rightarrow O$	k_9	8.0×10^{8}	s^{-1}	[10]
	Reactions for cyclohexene				
10	cyclohexene + $O_3 \rightarrow X_{2,CHEX} + 0.6OH$	k_{10}	7.80×10^{-17}	$cm^3\ molec^{-1}\ s^{-1}$	[11]
11	cyclohexene + $OH \rightarrow X_{1,CHEX}$	k_{11}	6.35×10^{-11}	$cm^3\ molec^{-1}\ s^{-1}$	[12]
12	$X_{2,CHEX} + OH \rightarrow X_{1,CHEX}$	k_{11}	6.35×10^{-11}	$cm^3\ molec^{-1}\ s^{-1}$	‡
13	$X_{1,CHEX} + OH \rightarrow X_{1,CHEX}$	k_{11}	6.35×10^{-11}	$cm^3\ molec^{-1}\ s^{-1}$	‡
	Reactions for hexanal				
14	hexanal + $OH \rightarrow X_{1,HEXAL}$	k_{14}	2.86×10^{-11}	$cm^3\ molec^{-1}\ s^{-1}$	[13]
15	$X_{1,HEXAL} + OH \rightarrow X_{1,HEXAL}$	k_{14}	2.86×10^{-11}	$cm^3\ molec^{-1}\ s^{-1}$	‡
	Reactions for indoor air scenario				
16	VOC2 + $O_3 \rightarrow X_2 + 0.86OH$	k_{16}	2.0×10^{-16}	$cm^3\ molec^{-1}\ s^{-1}$	[14]
17	VOC2 + $OH \rightarrow X_1$	k_{17}	1.71×10^{-10}	$cm^3\ molec^{-1}\ s^{-1}$	[14]
18	VOC1 + $OH \rightarrow X_1$	k_{18}	8.12×10^{-12}	$cm^3\ molec^{-1}\ s^{-1}$	†
19	$X_1 + OH \rightarrow X_1$	k_{18}	8.12×10^{-12}	$cm^3\ molec^{-1}\ s^{-1}$	‡
20	$X_2 + OH \rightarrow X_1$	k_{18}	8.12×10^{-12}	$cm^3\ molec^{-1}\ s^{-1}$	‡
21	$O_3 \rightarrow O_{3,\ wall}$	k_{21}	8.33×10^{-4}	s^{-1}	[15,16]

*I is the total fluence rate over a 222 nm light spectrum in $\mu W\ cm^{-2}$. See Figure S10.

[†]Calculated based on averaged VOC mixture (see Table S4).
[‡]Product VOCs are assumed to have the same OH reactivities as their precursors

Table S4: Table of components of the averaged VOC mixture (VOC1). The rate constants are weighted by the mole fraction to calculate an average OH rate constant for the mixture.

VOC	Mole fraction	Rate constant (cm^3 $molec^{-1}$ s^{-1})
HC3[*]	0.006	1.34×10^{-14}
HC8[†]	0.012	1.37×10^{-13}
Toluene	0.001	6.18×10^{-15}
Xylene	0.001	1.87×10^{-14}
Ethanol	0.038	1.21×10^{-13}
Isopropanol	0.018	9.08×10^{-14}
ketone	0.015	1.01×10^{-14}
formaldehyde	0.909	7.73×10^{-12}
VOC mixture (VOC1)	1	8.12×10^{-12}

[*]Straight-chain and branched alkanes up to C5[17]
[†]C6 and higher straight chain and branched alkanes, and all cycloalkanes[17]

S2.1. Calculation of indoor VOC mixture composition and emission rates

The lumped species VOC1 represents a mixture of compounds with a weighted average reactivity (see Table S4). We use the OH-reactive VOC mixture from Peng et al.,[17] and add formaldehyde in a 10:1 ratio (formaldehyde : total other VOC), giving formaldehyde concentrations (109 ppb) within the range of reported values from previous studies.[18]

The emission rates for VOC1 and VOC2 were calculated to match literature OH and O_3 reactivities for indoor spaces (30-50 s^{-1} for OH and 10-30x10^{-6} s^{-1} for O_3).[19] Using the rate constants for VOC1 and VOC2, this reactivity is achieved with 120 ppb VOC1 (49.2 s^{-1}) and 6 ppb VOC2 (29.5×10^{-6} s^{-1}). Price et al.[19] reports 0.7 hr^{-1} as a typical ventilation rate. By assuming the concentrations calculated above are for a ventilation rate of 0.7 hr^{-1}, we determine an emission rate from the concentration multiplied by the ventilation rate: 84 ppb hr^{-1} and 4.2 ppb hr^{-1} for VOC1 and VOC2, respectively.

S3. Additional Results and Discussion

S3.1. Ozone steady-state calculations

Steady-state ozone was measured in a clean chamber over a range of chamber dilution rates. These data allow comparison between the measured and modeled relationship between ventilation and steady-state ozone (See Figure 1 and Figure S3).

Dilution rates were measured using an exponential fit of the acetonitrile signal from the NH_4^+-CIMS. Steady-state concentrations were measured by fitting the ozone timeseries to equation S1:

$$[O_3](t) = \frac{P_{O_3}}{k}\left(1 - e^{-kt}\right) \qquad [S1]$$

where P_{O_3} is the production rate of ozone in ppb s^{-1} and *k* is the dilution rate constant in s^{-1}. The term $\frac{P_{O_3}}{k}$ is the steady-state ozone concentration.

These fits also provide the ozone production rate (PO_3 = 324 ± 18 ppb hr^{-1} (1σ)) and the dilution rate constant (k). P_{O3} is in reasonably good agreement with previous measurements[20] when differences in fluence rate are considered (e.g. 324 vs 22 ppb hr^{-1}, 45 vs 2 μW cm^{-2}). Using the chamber volume of 150 L, this ozone production rate can be expressed as 96 ± 5 μg hr^{-1}. This value is lower than the value reported in Peng et al.[20] but comparable to values reported by others.[21,22] As discussed in Peng et al., the ozone mass production rate increases approximately linearly with path length, which is significantly smaller in our experiments than in their 21 m^3 chamber. Normalizing the ozone mass production rate by the path length of 1.2 m gives 80 ± 4 μg hr^{-1} m^{-1}. This is about half of what was observed by Peng et al. but reasonable considering that a substantial fraction of the total 222 nm photons intersect the walls in our setup due to the tall and narrow dimensions of the chamber. The fitted dilution rate constant agrees well with the dilution rate as derived from the acetonitrile fits (slope = 1.06, R^2 = 0.99).

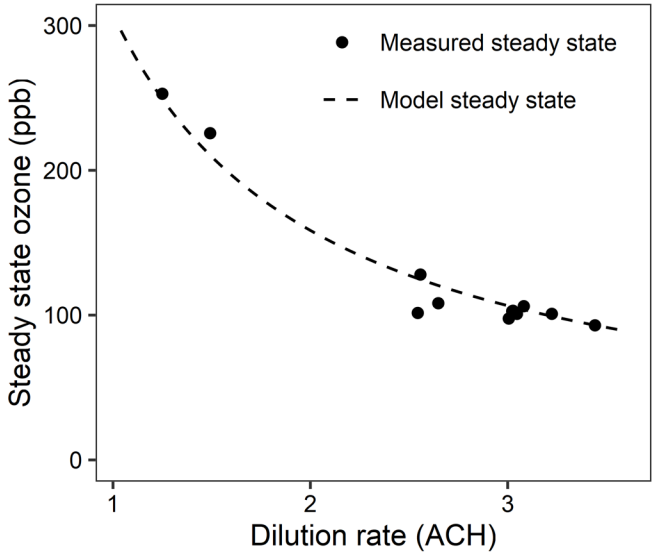

Figure S3: Measured and modeled steady-state ozone as a function of dilution rate. As noted previously, the modeled result shown here is independent of the measured points.

S3.2. Potential loss of VOCs via photolysis or deposition

Here we show that direct photolysis and wall loss are unlikely to contribute to observed VOC loss (Figure 2), meaning that all the observed loss is due to oxidation only.

Using literature absorption cross sections for pentanal (in the absence of data for hexanal at the relevant wavelengths)[23] and cyclohexene,[24] we estimate upper bounds for the photolysis rate constants as 3.2×10^{-8} s^{-1} and 1.6×10^{-5} s^{-1} which would account for 0.023% and ~2.7% total precursor loss under "base case" conditions. These represent upper limits, since the photolysis quantum yields may be below unity; thus photolytic loss does not contribute substantially to overall VOC loss.

Effective saturation mass concentrations for cyclohexene, hexanal, and acetonitrile are all $> 6 \times 10^{7}$ μg m^{-3}. Based on typical values for the equivalent mass concentration of the chamber walls, C_w, (10 – 30 mg m^3), these compounds should reside almost entirely (> 99.9%) in the gas-phase at equilibrium.[25] Considering also the short timescale of these experiments and the timescale of gas-wall partitioning, usually 10s of minutes,[25] vapor wall loss is expected to be an insignificant contributor to VOC loss.

We note some loss of hexanal for the reaction with O_3 in the absence of 222 nm light. While we anticipate no reaction of hexanal with O_3 and no formation of OH in these conditions, we observe a decay in the hexanal signal that is slightly (~3%) faster than the dilution tracer. While we can calculate an inferred $[OH]_{avg}$ based on these loss rates (see Table S1), we hypothesize that the loss of hexanal under these conditions is more likely due to minor loss pathways that are not explicitly accounted for in our analysis. While $[OH]_{avg}$ is greater than 0, the minimum value calculated is negative (Table S1), suggesting that this result may not be significant. In the O_3-only hexanal experiments, we also see evidence of some dilution-corrected ion signals growing in during the experiment (Figure S6), but most associated molecular formulas are not consistent with hexanal oxidation chemistry, suggesting that these ions are most likely background species, whose growth is due to small errors in the dilution correction or background subtraction procedure. Even if the precursor decay and the increase in dilution-corrected ion signals are due to oxidation chemistry, the total apparent oxidation is nonetheless small relative to all other VOC experiments.

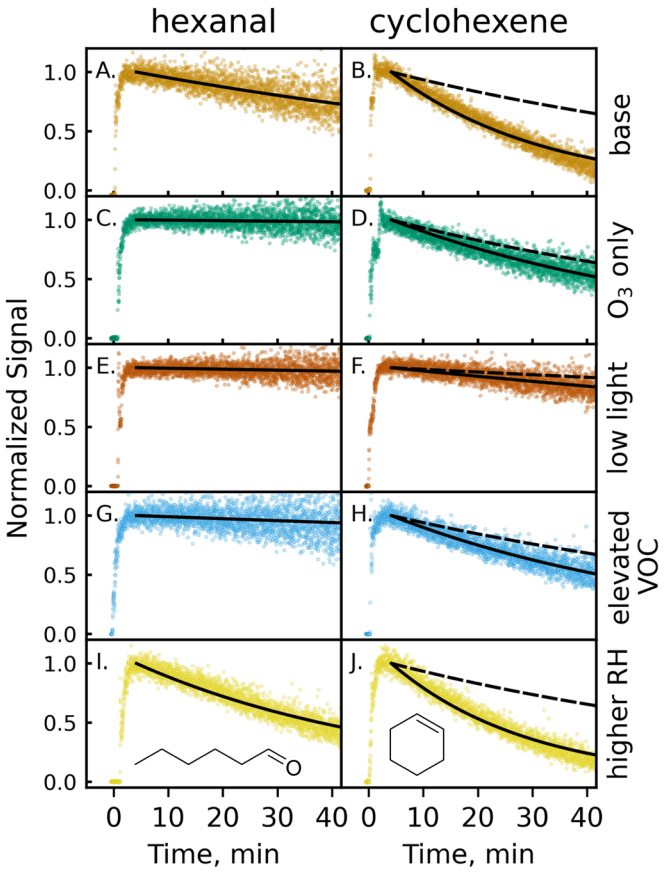

Figure S4: Normalized decays of hexanal and cyclohexene after introduction to the GUV_{222}-irradiated chamber for all five experimental conditions. Time 0 refers to when the VOC was injected into the chamber. Traces are background- and dilution-corrected, so observed decays are from oxidative loss. Details of each experimental condition (base, dark O_3, low light, elevated VOC, higher RH) are given in the text and Table S1. Solid black lines denote single-exponential fits to the observed decays; dashed black lines show the expected decay of cyclohexene from reaction with O_3 only.

S3.3. Elevated VOC and higher RH experiments

In addition to the three sets of conditions discussed in the main text (base conditions, O_3-only, and low light), experiments were performed with a higher VOC precursor concentration ("elevated VOC") and higher relative humidity ("higher RH").

When the VOC precursor concentration is increased from 10 to 100 ppb ("elevated VOC"), a slower decay of the precursor signal is observed (Figure S4). For hexanal, the observed decay rate decreases by about a factor of 5 compared to base conditions. The steady-state O_3 concentration is not substantially affected by the addition of the O_3 reactive VOC, but the observed excess reactivity for cyclohexene decreases by approximately a factor of 3 compared to base conditions. This is consistent with oxidation

by OH radicals; in the experiments, reaction with VOCs represents the main sink of OH radicals, so a higher initial VOC concentration results in a lower average OH concentration.

When RH is increased from 25% to 45%, substantially faster precursor decays are observed. For hexanal, experiments conducted at higher RH have a factor of 2.5 faster observed decay rate. For cyclohexene, the decay due to O_3 reaction is unchanged (O_3 concentrations are not RH dependent, as shown in Figure 1 and Table S1), but excess reactivity is increased by ~16%. This is again consistent with OH radical oxidation. The photolytic generation of OH (R5) is roughly linearly dependent on RH; hence, a near-proportional increase in the decay rate is observed for hexanal. However, the non-photolytic generation of OH (R3) is not RH dependent. For cyclohexene, this results in a smaller fractional increase in OH, and a more modest observed increase in excess reactivity.

S3.4. Calculation of average OH and range of OH concentrations

To calculate average OH concentrations, timeseries are normalized to the value at t = 250 s (the point at which the chamber has become homogeneously mixed) and the precursor signal is fit with a single exponential from t = 250 – 2500 s, according to the following functional forms:

$$[hexanal] = \exp\left(-k_{OH+hexanal}[OH]_{avg}(t - 250s)\right) \quad [S2]$$

$$[cyclohexene] = \exp\left(\left(-k_{O_3+cyclohexene}[O_3]_{avg} - k_{OH+cyclohexene}[OH]_{avg}\right)(t - 250s)\right) \quad [S3]$$

To calculate the range of [OH] observed over the course of the experiment, exponential fits are applied to a rolling 15-minute window and the minimum and maximum OH values are used as upper and lower error bars in Figure 3.

S3.5. Calculation of integrated product signals

To reduce the influence of changing [OH] on the interpretation of product ratios in Figure 4, ratios are calculated based on the average each ion timeseries, enabling appropriate comparison to average OH and O_3 oxidation rates in Figure 4B. To reduce the influence of any gaps in the data on the average signals, these calculations are performed using a numerical integral. Product timeseries are integrated from t = 250 – 2500 s and normalized to the total time-integrated mass spectrometric signal to calculate the fractional integrated signal (shown in Figure 4A). For Figure 4B, the ratio of the time-integrated signals for $C_6H_{10}O_2$ and $C_6H_{10}O_3$ (detected as $C_6H_{10}O_2NH_4^+$ and $C_6H_{10}O_3NH_4^+$) is used. To calculate the range of product ratios observed throughout the experiment, the integrals are also taken over a rolling 15-minute window and the minimum and maximum values are used as error bars in the y-direction in Figure 4B). Error bars representing the range of $k_{OH}[OH]$ / $k_{O3}[O_3]$ values in Figure 4B are calculated by propagating the OH range calculated above in Section S3.4 with the range of O_3 values measured during the experiment.

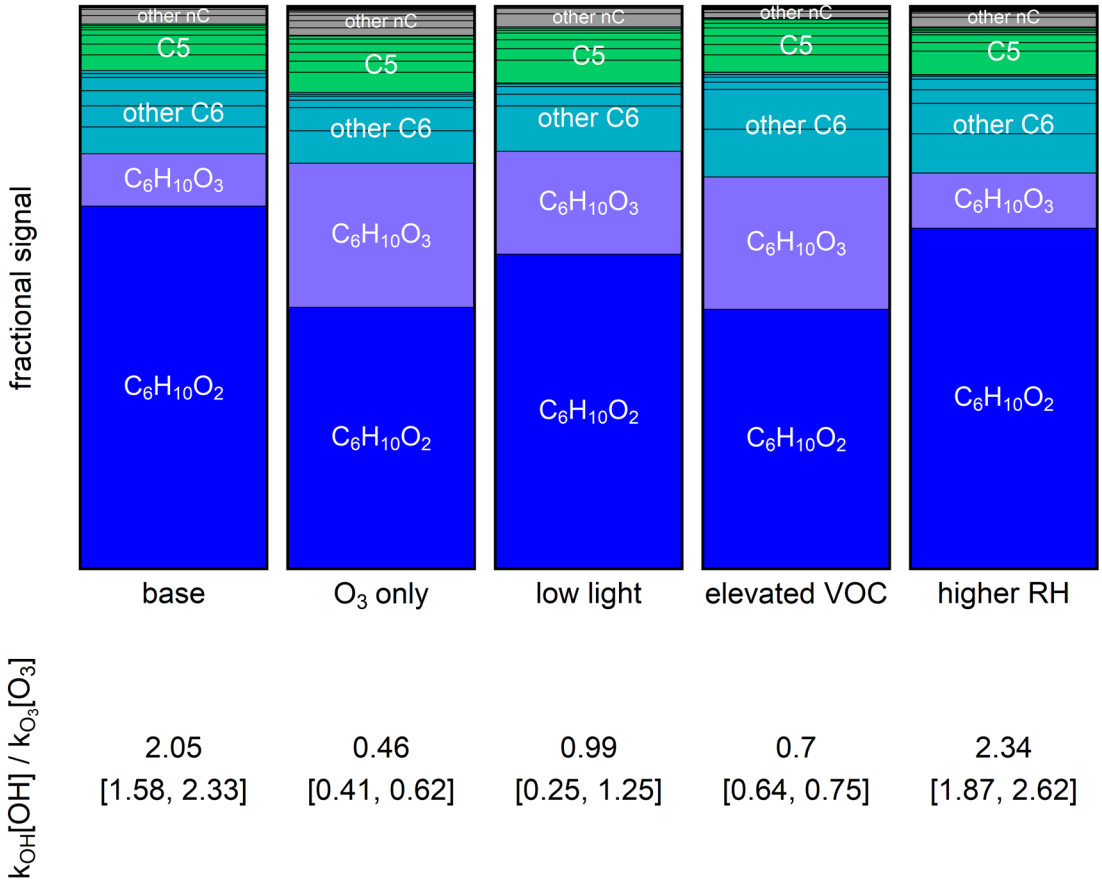

Figure S5: Gas-phase cyclohexene products for all five experiments. Product timeseries are integrated from t = 250-2500 s, normalized to the total integrated mass spectrometric signal, and sorted by carbon number (see Section S1.5). Note that instrument sensitivity may shift slightly with differing RH so the signal may not be directly comparable between the "higher RH" case and the other experiments. The ratio of the rates of OH and O_3 oxidation shown below the plot are the same as those plotted in Figure 4B; the values in the brackets represent the range of values observed throughout the experiment, as shown by the error bars in Figure 4B.

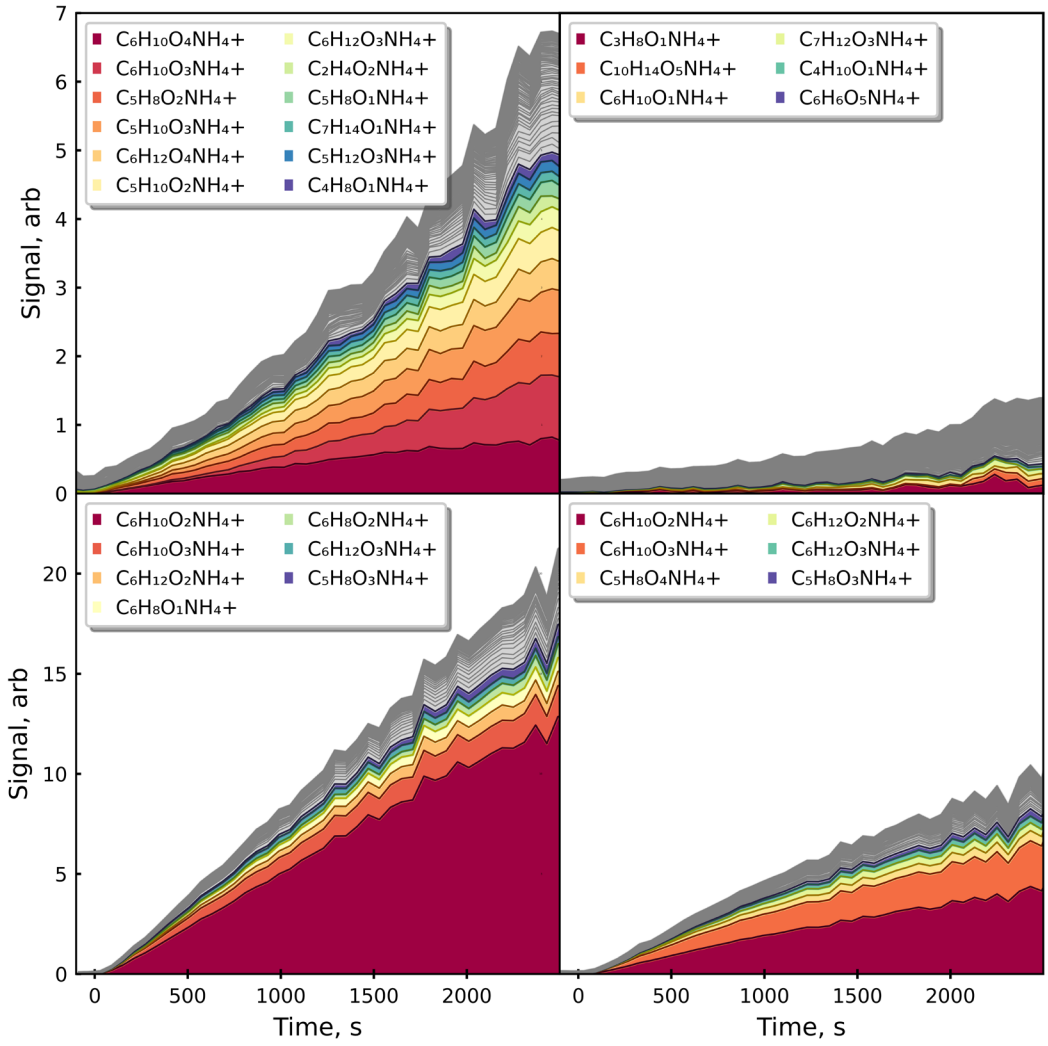

Figure S6: Products observed in the base conditions (left) and dark ozonolysis (right) experiments for hexanal (top panels) and cyclohexene (bottom panels). Products that account for >2% of the total product signal are colored and identified in the key. Signals are uncalibrated and scaled to the signal of the precursor, which differ slightly between the base case and dark experiments due to small variations in the injected precursor amount.

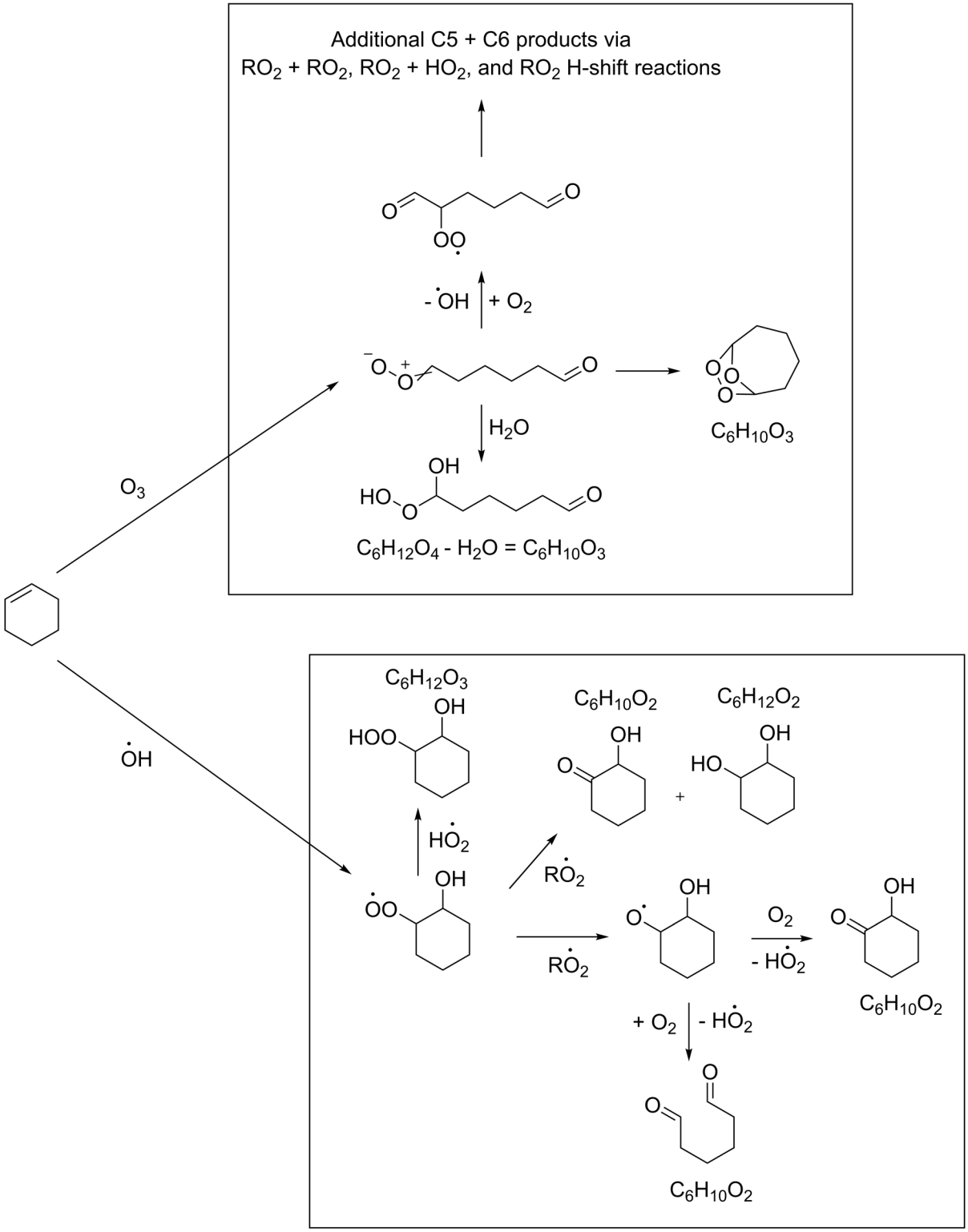

Scheme S1: Reaction scheme for cyclohexene oxidation. The loss of H_2O from multifunctional OVOCs is common in chemical ionization mass spectrometry, and explains one possible pathway to $C_6H_{10}O_3$.

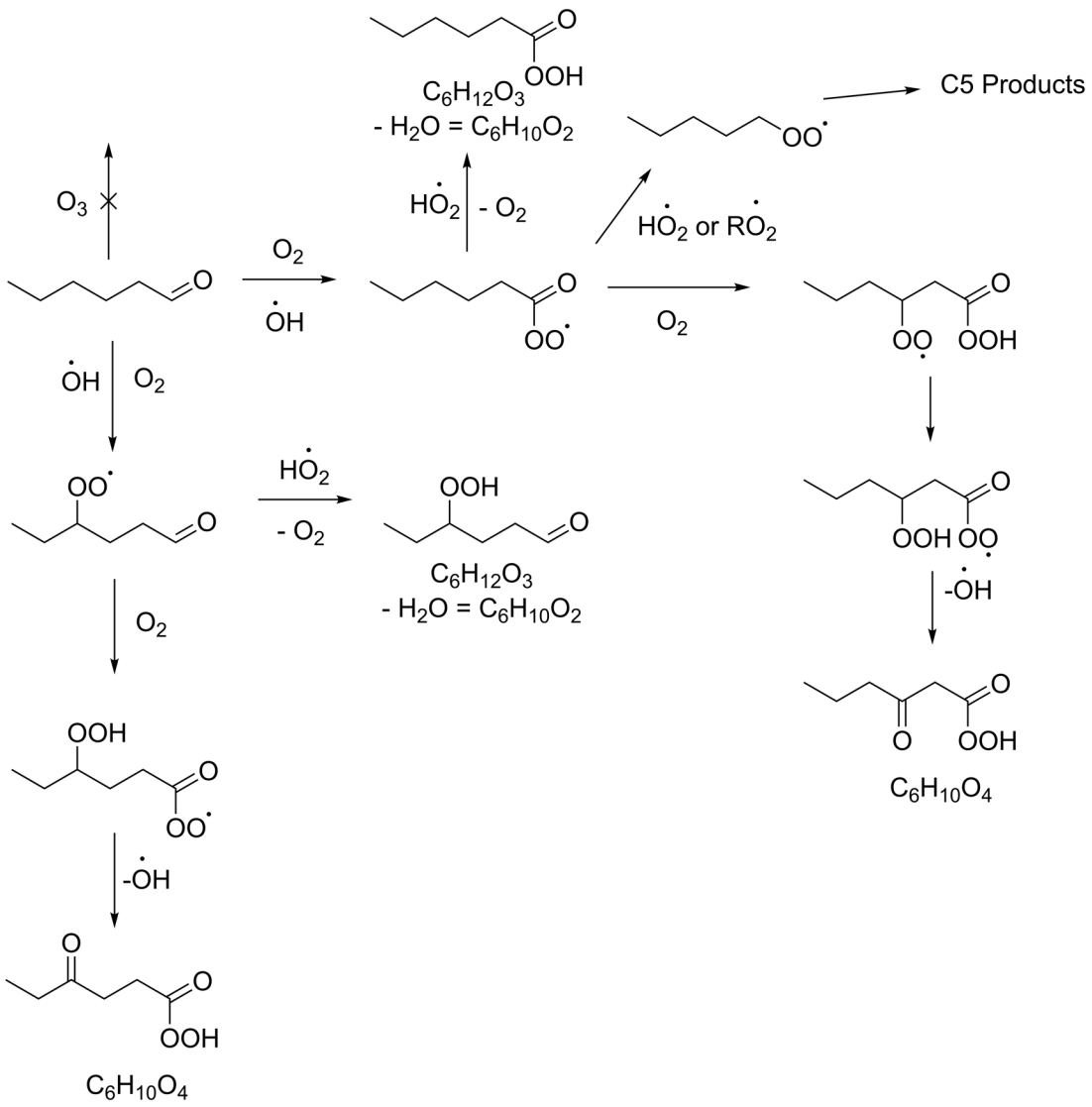

Scheme S2: Reaction scheme for hexanal oxidation. The loss of H_2O from multifunctional OVOCs is common in chemical ionization mass spectrometry, and explains two possible pathways to $C_6H_{10}O_2$.

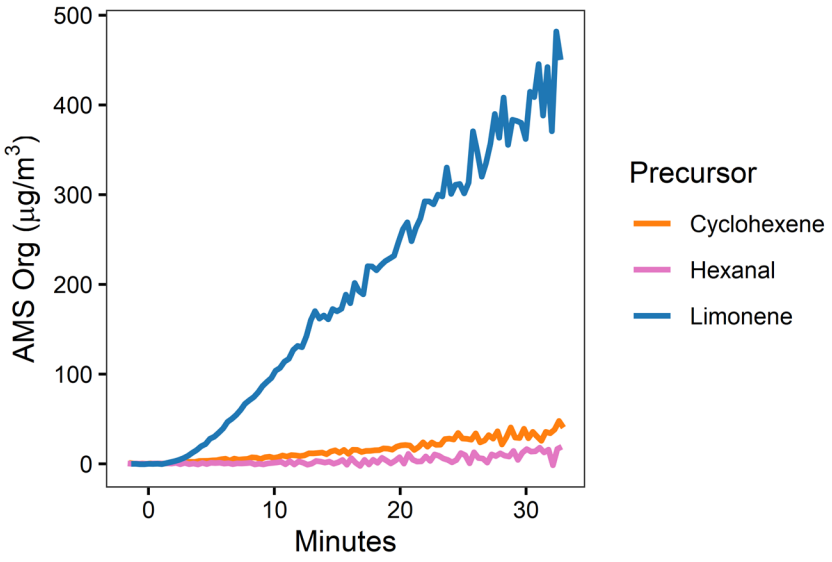

Figure S7: Dilution- and wall-loss-corrected timeseries of organic aerosol from cyclohexene, hexanal, and limonene at 100 ppb starting concentration.

S3.6. Nucleation of ultrafine particles

At full light intensity, 222 nm-driven nucleation of ultrafine particles is observed when particle concentrations are low (less than ~1 x 10^4 particles cm^{-3}) (See Figure S8E). This occurs even after the chamber has been flushed with clean air for > 30 lifetimes. Under these conditions, nucleated particles reach concentrations of 8-9 x 10^4 particles cm^{-3} after the lights are turned on, though total particle mass remains below 1.3 µg m^{-3} in all cases. In contrast, no nucleation is observed in the presence of O_3, OH from HONO photolysis at 340 nm, or attenuated 222 nm light.

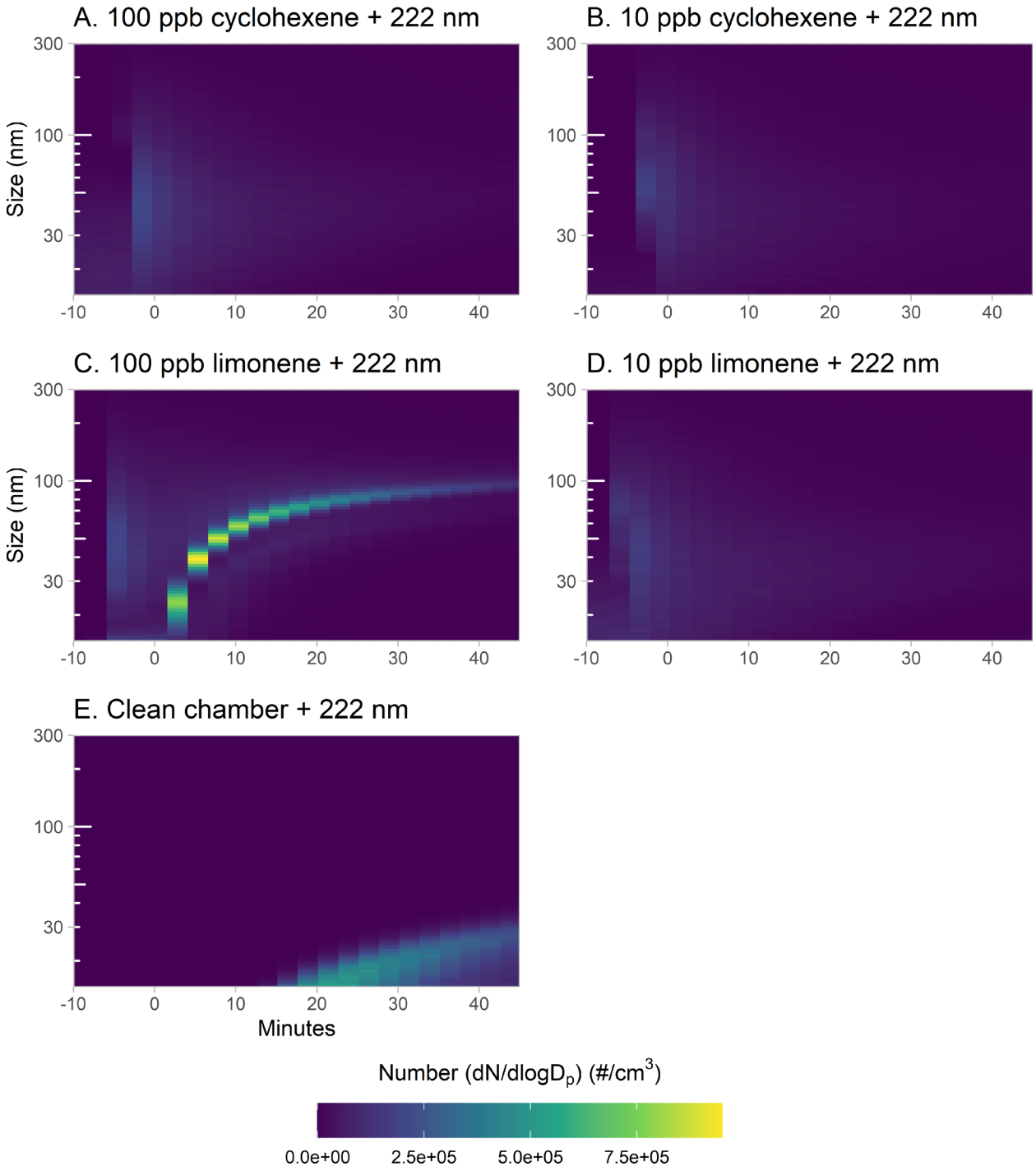

Figure S8: Particle number size distributions from selected experiments. No nucleation occurred during experiments where seed particles were added, with the exception of the 100 ppb limonene + 222 nm light experiment (Panel C). Panel E shows typical nucleation of ultrafine particles in a clean chamber after the 222 nm light was turned on. For each panel, time = 0 minutes corresponds to the time when the VOC was added or, for Panel E, the time at which the light was turned on. Seed particles were added at about time = -5 minutes.

S4. Extrapolation to Indoor Environments: Model Results

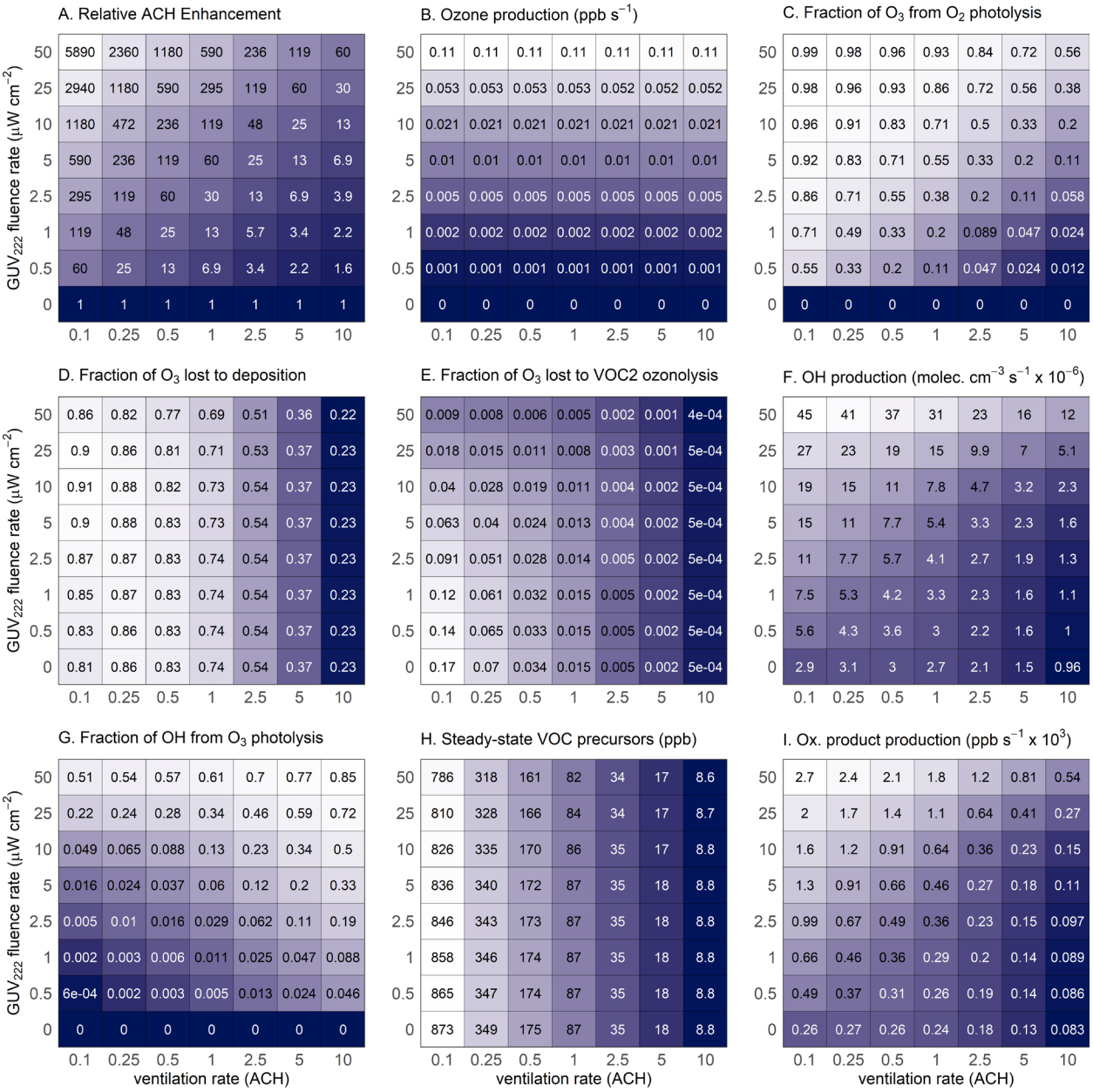

Figure S9: Additional outputs from the indoor environment model (see also Figure 5). Panel A shows the relative ACH enhancement calculated as the ratio of eACH and the real ACH due to ventilation. Panel B shows the production rate of O_3. Panel C shows the fraction of O_3 produced directly by 222 nm photolysis of O_2 (See R1-2 in the main text); the other source is O_3 introduced by ventilation. Panels D and E show the fraction of O_3 lost to deposition and reaction with VOC2 respectively. Panel F shows the production rate of OH. Panel G shows the fraction of OH produced directly by 222 nm photolysis of O_3 (See R4-5 in the main text); the other source is the ozonolysis of alkenes (R3 in the main text). Panel H shows the total steady-state concentration of the two VOC precursor species. Panel I shows the production rates of first-generation oxidation products. Note that the color scaling is different for each panel and is logarithmically scaled.

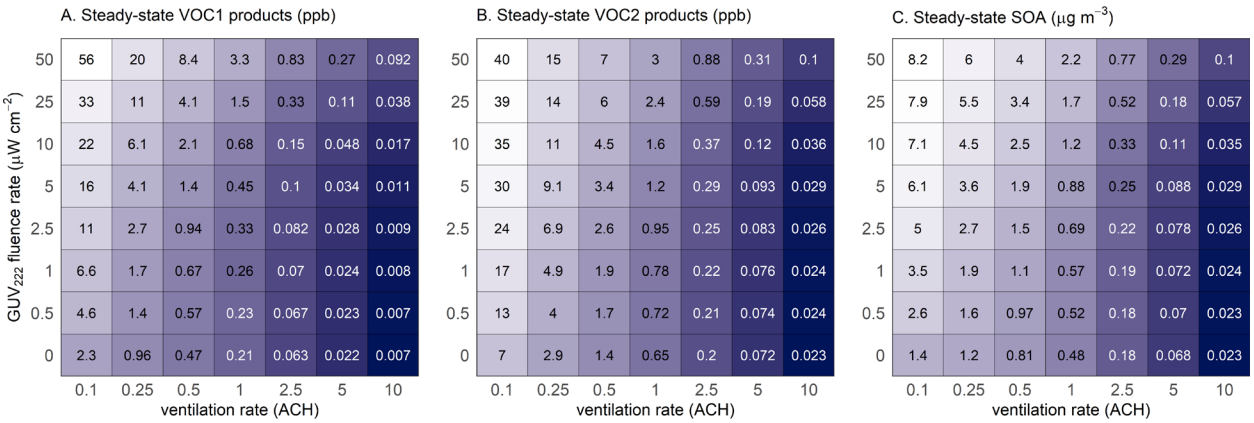

Figure S10: Steady-state concentrations of total oxidation products from the VOC1 (VOC mixture, see Table S4 and Section S2.1) (Panel A), VOC2 (based on limonene) (Panel B), and estimated steady-state secondary organic aerosol concentration (Panel C). Since the VOC mixture is mainly formaldehyde, it is assumed not to produce organic aerosol. Steady-state SOA is estimated based on the total concentration of VOC2 oxidation products, assuming a typical molecular weight of 250 g mol^{-1}, a molar aerosol yield of 10% (equivalent to an aerosol mass yield of ~18%), and an aerosol loss rate of 0.4 hr^{-1} [26].

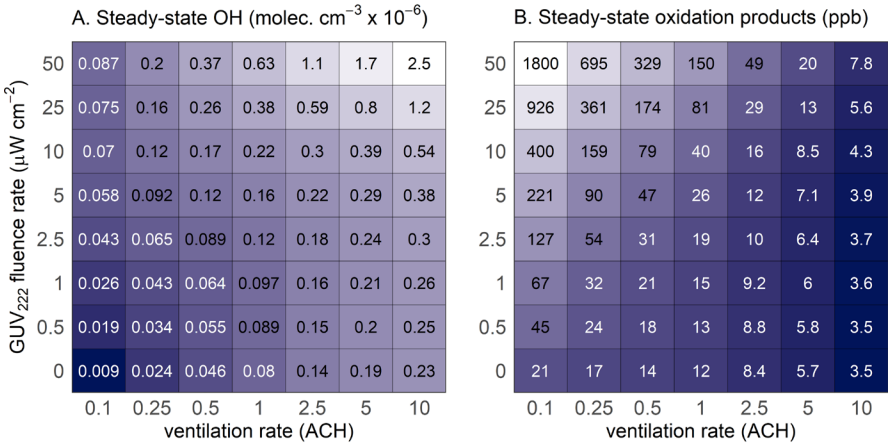

Figure S11: Outputs from the indoor environment model for a sensitivity study exploring the inclusion of the offgassing of OVOCs from the reaction of ozone with indoor surfaces. These model runs are exactly identical to those previously described in the main text, with the exception of the replacement of reaction 21 with $O_3 \rightarrow O_{3,\,wall} + 0.5X_1$, representing a 50% yield of volatilized OVOCs for each mole of ozone that deposits to surfaces. This yield is based off of measurements from the literature,[27,28] though we note that this is highly variable and uncertain. The plot shows steady-state concentrations of OH (Panel A) and organic oxidation products (Panel B) (compare to Figure 5). The addition of OVOC offgassing produces dramatic increases in steady state oxidation products, and moderate decreases in steady state OH. All other parameters show little or no change.

S4.1. Inclusion of NO_X cycling

While experiments were conducted under low NO_X conditions, indoor environments can have elevated NO_X levels,[29] which may facilitate radical propagation and further oxidation of VOCs. Since key NO_X cycling reactions, such as the photolysis of NO_2 and HONO, are highly uncertain in the presence of 222 nm light, we added a simple representation of NO_X radical cycling to the model which does not explicitly define NO_X concentrations. This model assumes that OH is recycled each time it reacts with a VOC, as can be demonstrated in a simple NO_X reaction scheme (RH + **OH** $\rightarrow$ $RO_2 + H_2O$, $RO_2 + NO \rightarrow RO + NO_2$, $RO + O_2 \rightarrow$ R'CHO + HO_2, $HO_2 + NO \rightarrow$ **OH** + NO_2). While this is likely an upper bound for OH recycling, it serves to show the general trend expected for the addition of NO_X chemistry to the system. As shown in Table S5, reactions 17-20 now recycle OH, and reaction 22 represents a sink of OH via reaction with a fixed 10 ppb of NO_2. This has the effect of substantially raising OH levels and increasing the production of OVOCs (Figure S12).

Table S5: List of reactions modified from Table S3 to include a simple representation of NO_X cycling in the 0-D box model. Reactions 17-20 include OH as both a reactant and a product. Reaction 22 is added to represent a sink of OH via reaction with a fixed level of NO_2.

Reaction number	Reaction	Rate ID	Rate	Unit	Note
17	VOC2 + OH $\rightarrow$ X_1 + OH	k_{17}	1.71×10^{-10}	$cm^3\ molec^{-1}\ s^{-1}$	-
18	VOC1 + OH $\rightarrow$ X_1 + OH	k_{18}	8.12×10^{-12}	$cm^3\ molec^{-1}\ s^{-1}$	-
19	X_1 + OH $\rightarrow$ X_1 + OH	k_{18}	8.12×10^{-12}	$cm^3\ molec^{-1}\ s^{-1}$	-
20	X_2 + OH $\rightarrow$ X_1 + OH	k_{18}	8.12×10^{-12}	$cm^3\ molec^{-1}\ s^{-1}$	-
22	OH + $NO_2 \rightarrow HNO_3$	k_{22}	2.71	s^{-1}	*

* $[NO_2]$ is fixed at 10 ppb based on Vardoulakis et al.[29] The fixed rate constant embeds this assumption with the JPL rate recommendation.[3]

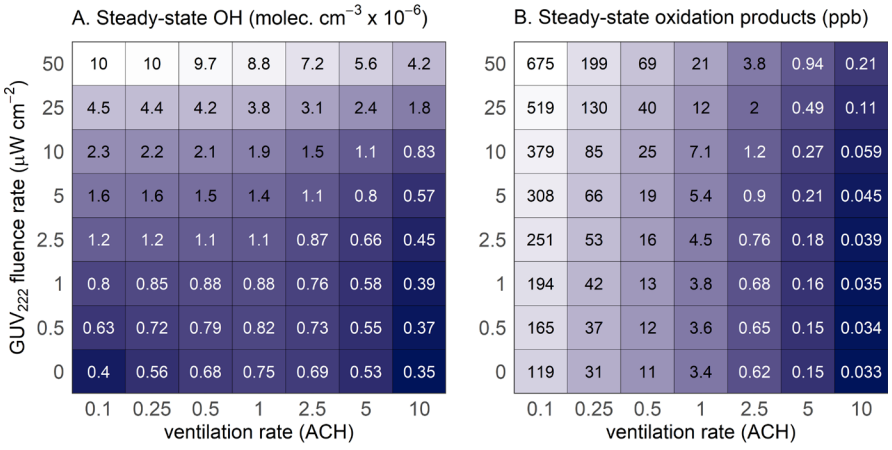

Figure S12: Outputs from the indoor environment model for a sensitivity study exploring the inclusion of a simple parameterization for NO_X cycling. These model runs are exactly identical to those previously described in the main text, with the exception of the use of the reactions shown in Table S5 in place of their counterparts in Table S3. The plot shows steady-state concentrations of OH (Panel A) and organic oxidation products (Panel B) (compare to Figure 5).

S4.2. Calculation of Effective Air Changes per Hour

Effective air changes per hour (eACH, Figure 5A) is defined based on both the ventilation rate and the SARS-CoV-2 viral inactivation rate (3.27 cm^2 mJ^{-1} [30]), along with the intensity of the GUV_{222}, according to equation S4:

$$eACH\ \left(\frac{1}{hr}\right) = ACH\ \left(\frac{1}{hr}\right) + 3.27\ \left(\frac{cm^2}{mJ}\right) * Fluence\ rate\left(\frac{\mu W}{cm^2}\right) * \left(\frac{mJ}{1000\ \mu J}\right) * \left(\frac{3600\ s}{hr}\right) \qquad [S4]$$

S5. References

(1) Ushio, Inc. Care222 Technical Specification Sheet. https://www.ushio.com/files/specifications/care222-filtered-far-uv-c-excimer-lamp-module-technical-data-sheet.pdf (accessed 2023-05-03).

(2) Blatchley, E. R.; Brenner, D.; Claus, H.; Cowan, T. E.; Linden, K.; Liu, Y.; Mao, T.; Park, S.-J.; Simons, R.; Sliney, D. *Far UV-C Radiation: Current State-of Knowledge*; White paper; International Ultraviolet Association Task Force.

(3) Burkholder, J.; Sander, S. P.; Abbatt, J. P. D.; Barker, J. R.; Cappa, C.; Crounse, J. D.; Dibble, T. S.; Huie, R. E.; Kolb, C. E.; Kurylo, M. J.; Orkin, V. L.; Percival, C. J.; Wilmouth, D. M.; Wine, P. H. *Chemical Kinetics and Photochemical Data for Use in Atmospheric Studies*; 19–5; NASA Jet Propulsion Laboratory, 2020.

(4) Krechmer, J.; Lopez-Hilfiker, F.; Koss, A.; Hutterli, M.; Stoermer, C.; Deming, B.; Kimmel, J.; Warneke, C.; Holzinger, R.; Jayne, J.; Worsnop, D.; Fuhrer, K.; Gonin, M.; de Gouw, J. Evaluation of a New Reagent-Ion Source and Focusing Ion–Molecule Reactor for Use in Proton-Transfer-Reaction Mass Spectrometry. *Anal. Chem.* **2018**, *90* (20), 12011–12018. https://doi.org/10.1021/acs.analchem.8b02641.

(5) Zaytsev, A.; Breitenlechner, M.; Koss, A. R.; Lim, C. Y.; Rowe, J. C.; Kroll, J. H.; Keutsch, F. N. Using Collision-Induced Dissociation to Constrain Sensitivity of Ammonia Chemical Ionization Mass Spectrometry (NH4+ CIMS) to Oxygenated Volatile Organic Compounds. *Atmos. Meas. Tech.* **2019**, *12* (3), 1861–1870. https://doi.org/10.5194/amt-12-1861-2019.

(6) DeCarlo, P. F.; Kimmel, J. R.; Trimborn, A.; Northway, M. J.; Jayne, J. T.; Aiken, A. C.; Gonin, M.; Fuhrer, K.; Horvath, T.; Docherty, K. S.; Worsnop, D. R.; Jimenez, J. L. Field-Deployable, High-Resolution, Time-of-Flight Aerosol Mass Spectrometer. *Anal. Chem.* **2006**, *78* (24), 8281–8289. https://doi.org/10.1021/ac061249n.

(7) Holzinger, R. PTRwid: A New Widget Tool for Processing PTR-TOF-MS Data. *Atmos. Meas. Tech.* **2015**, *8* (9), 3903–3922. https://doi.org/10.5194/amt-8-3903-2015.

(8) Koss, A. R.; Canagaratna, M. R.; Zaytsev, A.; Krechmer, J. E.; Breitenlechner, M.; Nihill, K. J.; Lim, C. Y.; Rowe, J. C.; Roscioli, J. R.; Keutsch, F. N.; Kroll, J. H. Dimensionality-Reduction Techniques for Complex Mass Spectrometric Datasets: Application to Laboratory Atmospheric Organic Oxidation Experiments. *Atmos. Chem. Phys.* **2020**, *20* (2), 1021–1041. https://doi.org/10.5194/acp-20-1021-2020.

(9) Wang, N.; Jorga, S. D.; Pierce, J. R.; Donahue, N. M.; Pandis, S. N. Particle Wall-Loss Correction Methods in Smog Chamber Experiments. *Atmos. Meas. Tech.* **2018**, *11* (12), 6577–6588. https://doi.org/10.5194/amt-11-6577-2018.

(10) Saunders, S. M.; Jenkin, M. E.; Derwent, R. G.; Pilling, M. J. Protocol for the Development of the Master Chemical Mechanism, MCM v3 (Part A): Tropospheric Degradation of Non-Aromatic

Volatile Organic Compounds. *Atmospheric Chemistry and Physics* **2003**, *3* (1), 161–180. https://doi.org/10.5194/acp-3-161-2003.
(11) Stewart, D. J.; Almabrok, S. H.; Lockhart, J. P.; Mohamed, O. M.; Nutt, D. R.; Pfrang, C.; Marston, G. The Kinetics of the Gas-Phase Reactions of Selected Monoterpenes and Cyclo-Alkenes with Ozone and the NO3 Radical. *Atmospheric Environment* **2013**, *70*, 227–235. https://doi.org/10.1016/j.atmosenv.2013.01.036.
(12) Aschmann, S. M.; Arey, J.; Atkinson, R. Kinetics and Products of the Reactions of OH Radicals with Cyclohexene, 1-Methyl-1-Cyclohexene, *Cis* -Cyclooctene, and *Cis* -Cyclodecene. *J. Phys. Chem. A* **2012**, *116* (38), 9507–9515. https://doi.org/10.1021/jp307217m.
(13) D'Anna, B.; Andresen, Ø.; Gefen, Z.; J. Nielsen, C. Kinetic Study of OH and NO 3 Radical Reactions with 14 Aliphatic Aldehydes. *Physical Chemistry Chemical Physics* **2001**, *3* (15), 3057–3063. https://doi.org/10.1039/B103623H.
(14) Calvert, J. G. *The Mechanisms of Atmospheric Oxidation of the Alkenes*; Oxford University Press, 2000.
(15) Grøntoft, T.; Raychaudhuri, M. R. Compilation of Tables of Surface Deposition Velocities for O3, NO2 and SO2 to a Range of Indoor Surfaces. *Atmospheric Environment* **2004**, *38* (4), 533–544. https://doi.org/10.1016/j.atmosenv.2003.10.010.
(16) Nazaroff, W. W.; Weschler, C. J. Indoor Ozone: Concentrations and Influencing Factors. *Indoor Air* **2022**, *32* (1). https://doi.org/10.1111/ina.12942.
(17) Peng, Z.; Miller, S. L.; Jimenez, J. L. Model Evaluation of Secondary Chemistry Due to Disinfection of Indoor Air with Germicidal Ultraviolet Lamps. *Environ. Sci. Technol. Lett.* **2023**, *10* (1), 6–13. https://doi.org/10.1021/acs.estlett.2c00599.
(18) Salthammer, T.; Mentese, S.; Marutzky, R. Formaldehyde in the Indoor Environment. *Chem. Rev.* **2010**, *110* (4), 2536–2572. https://doi.org/10.1021/cr800399g.
(19) Price, D. J.; Day, D. A.; Pagonis, D.; Stark, H.; Algrim, L. B.; Handschy, A. V.; Liu, S.; Krechmer, J. E.; Miller, S. L.; Hunter, J. F.; de Gouw, J. A.; Ziemann, P. J.; Jimenez, J. L. Budgets of Organic Carbon Composition and Oxidation in Indoor Air. *Environ. Sci. Technol.* **2019**, *53* (22), 13053–13063. https://doi.org/10.1021/acs.est.9b04689.
(20) Peng, Z.; Day, D.; Symonds, G.; Jenks, O.; Stark, H.; Handschy, A.; Gouw, J. de; Jimenez, J. Significant Production of Ozone from Germicidal UV Lights at 222 Nm. medRxiv May 16, 2023, p 2023.05.13.23289946. https://doi.org/10.1101/2023.05.13.23289946.
(21) Blatchley, E. R.; Brenner, D. J.; Claus, H.; Cowan, T. E.; Linden, K. G.; Liu, Y.; Mao, T.; Park, S.-J.; Piper, P. J.; Simons, R. M.; Sliney, D. H. Far UV-C Radiation: An Emerging Tool for Pandemic Control. *Critical Reviews in Environmental Science and Technology* **2023**, *53* (6), 733–753. https://doi.org/10.1080/10643389.2022.2084315.
(22) Ma, B.; Burke-Bevis, S.; Tiefel, L.; Rosen, J.; Feeney, B.; Linden, K. G. Reflection of UVC Wavelengths from Common Materials during Surface UV Disinfection: Assessment of Human UV Exposure and Ozone Generation. *Science of The Total Environment* **2023**, *869*, 161848. https://doi.org/10.1016/j.scitotenv.2023.161848.
(23) Tadić, J.; Juranić, I.; Moortgat, G. K. Pressure Dependence of the Photooxidation of Selected Carbonyl Compounds in Air: N-Butanal and n-Pentanal. *Journal of Photochemistry and Photobiology A: Chemistry* **2001**, *143* (2), 169–179. https://doi.org/10.1016/S1010-6030(01)00524-X.
(24) Doner, A. C.; Christianson, M. G.; Davis, J. C.; Koritzke, A. L.; Larsson, A.; Frandsen, K.; Rotavera, B. Vacuum-Ultraviolet Absorption Cross-Sections of Functionalized Cyclic Hydrocarbons: Six-Membered Rings. *Journal of Quantitative Spectroscopy and Radiative Transfer* **2019**, *236*, 106603. https://doi.org/10.1016/j.jqsrt.2019.106603.

(25) Krechmer, J. E.; Pagonis, D.; Ziemann, P. J.; Jimenez, J. L. Quantification of Gas-Wall Partitioning in Teflon Environmental Chambers Using Rapid Bursts of Low-Volatility Oxidized Species Generated in Situ. *Environ. Sci. Technol.* **2016**, *50* (11), 5757–5765. https://doi.org/10.1021/acs.est.6b00606.
(26) Boedicker, E. K.; Emerson, E. W.; McMeeking, G. R.; Patel, S.; Vance, M. E.; Farmer, D. K. Fates and Spatial Variations of Accumulation Mode Particles in a Multi-Zone Indoor Environment during the HOMEChem Campaign. *Environ. Sci.: Processes Impacts* **2021**, *23* (7), 1029–1039. https://doi.org/10.1039/D1EM00087J.
(27) Wang, H.; Morrison, G. Ozone-Surface Reactions in Five Homes: Surface Reaction Probabilities, Aldehyde Yields, and Trends. *Indoor Air* **2010**, *20* (3), 224–234. https://doi.org/10.1111/j.1600-0668.2010.00648.x.
(28) Wisthaler, A.; Weschler, C. J. Reactions of Ozone with Human Skin Lipids: Sources of Carbonyls, Dicarbonyls, and Hydroxycarbonyls in Indoor Air. *Proceedings of the National Academy of Sciences* **2010**, *107* (15), 6568–6575. https://doi.org/10.1073/pnas.0904498106.
(29) Vardoulakis, S.; Giagloglou, E.; Steinle, S.; Davis, A.; Sleeuwenhoek, A.; Galea, K. S.; Dixon, K.; Crawford, J. O. Indoor Exposure to Selected Air Pollutants in the Home Environment: A Systematic Review. *IJERPH* **2020**, *17* (23), 8972. https://doi.org/10.3390/ijerph17238972.
(30) Ma, B.; Linden, Y. S.; Gundy, P. M.; Gerba, C. P.; Sobsey, M. D.; Linden, K. G. Inactivation of Coronaviruses and Phage Phi6 from Irradiation across UVC Wavelengths. *Environ. Sci. Technol. Lett.* **2021**, *8* (5), 425–430. https://doi.org/10.1021/acs.estlett.1c00178.